RESEARCH

Modeling genotypes in their microenvironment to predict single- and multi-cellular behavior

Dimitrios Voukantsis [1], Kenneth Kahn [1,2], Martin Hadley [2], Rowan Wilson [2] and Francesca M. Buffa [1,*]

[1]Computational Biology and Integrative Genomics, MRC/CRUK Oxford Institute, Departmemt of Oncology, University of Oxford, Old Road Campus, Oxford, Oxfordshire, OX3 7DQ, UK and [2]Academic Information Technology Research Team, University of Oxford, 13 Bambury Road, Oxford, Oxfordshire, OX2 6NN, UK

*Correspondence address. Francesca M. Buffa, MRC/CRUK Oxford Institute, Department of Oncology, University of Oxford, Old Road Campus, Oxford, Oxfordshire, OX3 7DQ, UK. E-mail: francesca.buffa@oncology.ox.ac.uk http://orcid.org/0000-0003-0409-406X

Abstract

A cell's phenotype is the set of observable characteristics resulting from the interaction of the genotype with the surrounding environment, determining cell behavior. Deciphering genotype-phenotype relationships has been crucial to understanding normal and disease biology. Analysis of molecular pathways has provided an invaluable tool to such understanding; however, typically it does not consider the physical microenvironment, which is a key determinant of phenotype.

In this study, we present a novel modeling framework that enables the study of the link between genotype, signaling networks, and cell behavior in a three-dimensional microenvironment. To achieve this, we bring together Agent-Based Modeling, a powerful computational modeling technique, and gene networks. This combination allows biological hypotheses to be tested in a controlled stepwise fashion, and it lends itself naturally to model a heterogeneous population of cells acting and evolving in a dynamic microenvironment, which is needed to predict the evolution of complex multi-cellular dynamics. Importantly, this enables modeling co-occurring intrinsic perturbations, such as mutations, and extrinsic perturbations, such as nutrient availability, and their interactions.

Using cancer as a model system, we illustrate how this framework delivers a unique opportunity to identify determinants of single-cell behavior, while uncovering emerging properties of multi-cellular growth.

This framework is freely available at http://www.microc.org.

Keywords: signaling networks; gene networks; molecular pathways; genotype to phenotype; agent-based modeling; microenvironment; executable biology

Introduction

A comprehensive understanding of living organisms, including their development and the occurrence and progression of disease, requires systematic efforts into deciphering the link between the multitude of different genotypes and phenotypes that is the set of observable characteristics resulting from the interaction of the genotype with the surrounding environment, determining cell morphology and behavior.

Efforts to characterize such relationships have proliferated in recent years thanks, in part, to the increased capability to efficiently collect the necessary data in an ever increasing number of organisms and individuals. Such efforts have spanned from cataloguing genetic variation in thousands of individuals [see, e.g., 1] and searching for genotype-phenotype associations, to silencing or inactivating thousands of genes in laboratory high-throughput screens to study their function [see, e.g., 2]. How-

ever, efficient instruments to achieve a comprehensive understanding of the causal nexus between a given genotype and the observed phenotype are still lacking, and this is particularly true when such a nexus is complex and multifactorial [3–5]. One promising means to achieve such an understanding has been the characterization and modeling of biological pathways [5].

Several of the key biological pathways regulating cellular function are increasingly understood, along with their dysregulation in multiple diseases [6–9]. However, much less is known about how these pathways interact and determine the behavior of individual cells and multi-cellular systems. This has fueled methodological development of efficient representations of such interactions in order to facilitate the study of the underlying potential mechanisms. A number of different approaches have been proposed, including modeling by differential equations and network modeling methods, such as petri nets and logical networks [10–12]. Such methods have produced encouraging results [13–16], but it is becoming increasingly evident that modeling molecular pathways and signaling, or gene, networks in isolation, dissociated from the cellular context, does not reflect the crucial impact of the microenvironment in determining the phenotype [17–19]. Additionally, as single-cell sequencing and imaging technologies are providing new in-depth information about the genotype and phenotype of single, or small groups of, cells [20], modeling approaches that enable consideration of cells both as independent entities and as a population are becoming increasingly attractive.

To address the above needs, we developed a novel computational framework that combines Agent-Based Modeling (ABM) and gene network modeling. This framework tackles the fundamental challenge of integrating genotype with phenotype data while accounting for certain important aspects of the physical microenvironment, a key determinant of the phenotype. The most innovative aspect of this framework is that it makes it possible to build models of the genotype-phenotype relationship in a three-dimensional (3D) spatially aware microenvironment, including aspects such as signaling to and from the microenvironment and signaling between cells. Importantly, the collective behavior and evolution of cellular populations emerges from the properties and behavior of individual cells, which in turn are governed by the underlying dynamics of specific signaling networks and the interactions with the surrounding cells and microenvironment. This permits to predict the behavior of individual cells, and the entire population of cells, and it also makes it possible to study of the causative mechanisms of such behavior.

Here, we introduce this modeling framework, illustrate the capabilities of microC, a first cloud-based implementation of the framework, and we illustrate the range of potential applications that it enables. Specifically, we perform perturbation experiments of increasing complexity in which we monitor over time the 3D growth and evolution of mixed populations of cells.

To achieve this, we chose the example of cancer: a complex disease where methods to study the link between genotype and phenotype are particularly and urgently needed [4]. To inform our choices for the gene network and the model parameters, we exploited previously acquired data on gene interactions and cell growth from a number of independent publications. We then built our initial model in a mechanistic "bottom-up" fashion, progressing from the individual elements to the whole system. Following this strategy, we simulated the 3D growth of cell spheroids focusing on pathways underlying the main hallmarks of cancer, including sustained proliferative signals, resistance to cell death, and evasion of growth suppressors [9].

We thus considered a set of alterations among the most frequently observed across all cancer types, namely, epidermal growth factor receptor (EGFR) activation, p53 loss-of-function, and phosphatase and tensin homolog (PTEN) loss-of-function [21]. We then asked to what extent this initial model, which has been built based on general assumptions and not optimized for a specific cancer type, could reproduce experimental results not used for the model construction and obtained in a cancer that often displays these mutations. For this we chose basal-like triple-negative breast cancer. This type of breast cancer lacks receptors for the hormones estrogen, progesterone, and the Her2 protein, and thus is not responsive to treatments targeting these. Importantly, an immortal though not tumorigenic mammary tumor cell line exists, MCF10A, which is considered a suitable pre-malignant model [22], allowing us to assess the effect of inducing these alterations as single drivers, or together.

With this model, we gradually increased the complexity of our simulations to investigate the effect that varying genetic and microenvironmental parameters has on the model predictions and on the resulting clonal competition, signaling to and from the microenvironment, and cell-cell interaction.

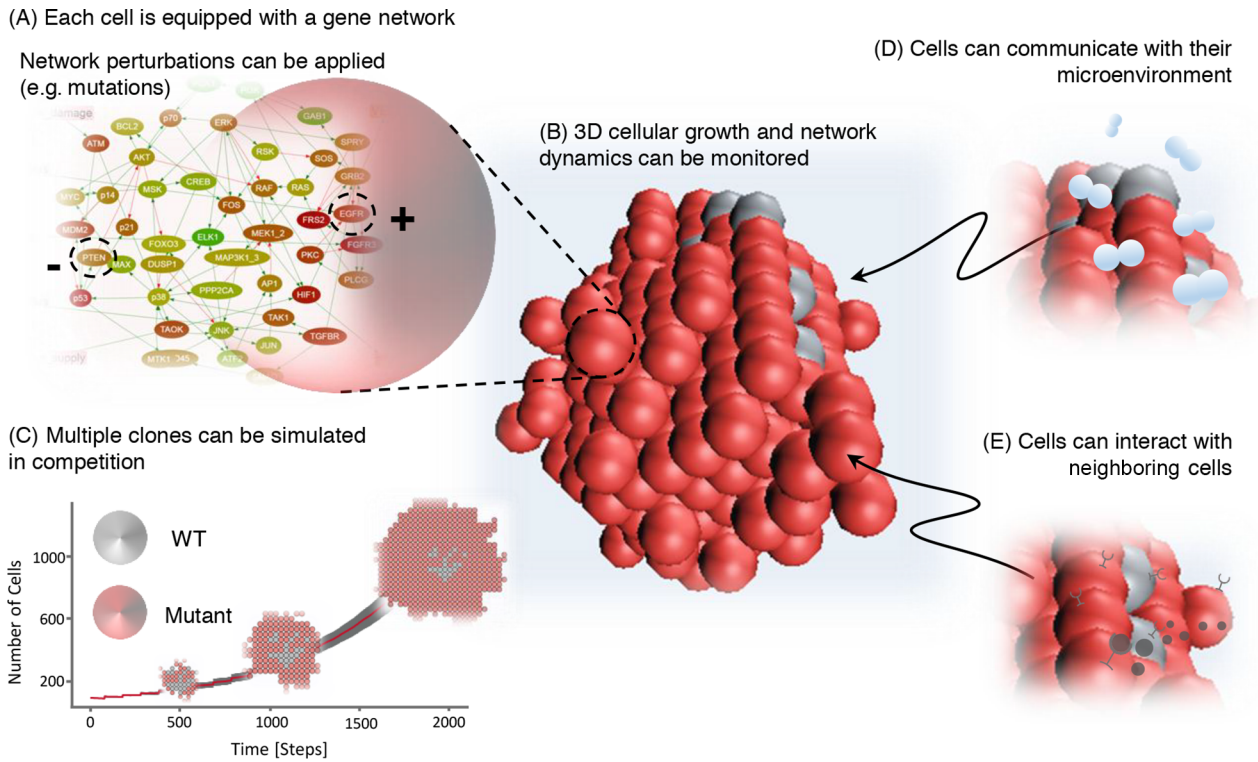## Methods: the microC Framework

Rationale for the framework

Previous studies have modeled cells as computational agents and started to consider replacing ABM conditional statements that drive cellular behavior with gene networks that can more realistically represent the dynamical features of the intracellular system. In particular, small-scale predefined logical networks have been used to model the cell-cycle arrest in a model of avascular spheroid growth [23] and to study cell differentiation in a hyper-sensitivity reaction model [24]. However, these networks were considered as static entities, providing simple rules and not fully embedded in the ABM simulation. In another example, cells have been equipped with relatively more complex decision-making models, represented as differential equations [25], but this approach was also not fully embedded in the ABM and is further limited by the requirement of prior knowledge for the many kinetic parameters to represent pathways accurately.

microC fully exploits ABM technology. Specifically, the cellular behavior is determined by a gene network, encapsulated within the cell, and by the interactions of the gene network with the surrounding microenvironment (Fig. 1). Both the cells and the inner networks are simulated using ABM. As a result, cellular behavior may be studied both at the single-cell level, decoding the link between a cell genotype and its phenotypic realization in a given contextual environment, and also at the more global level, allowing the search for emerging properties of the multicellular system.

Key elements of the framework

To define a specific model in the microC modeling framework, a number of inputs and parameter values need to be provided. These define the environment of the simulation, some of the cell's characteristics, the number of replicates considered in each simulation and the length of the simulation, the choice of the gene network, the cell mutation profiles, and how a cell interacts with the environment and other cells. These parameters and how they define the specific models are presented below and discussed further in the microC protocol available via the Protocol.IO repository [26]. Of note, in this work, we set the pa-

(A) Each cell is equipped with a gene network

Network perturbations can be applied
(e.g. mutations)

(D) Cells can communicate with their
microenvironment

(B) 3D cellular growth and network
dynamics can be monitored

(E) Cells can interact with
neighboring cells

(C) Multiple clones can be simulated
in competition

WT

Mutant

Figure 1: Conceptual representation of microC environment and simulation components. The microC framework enables multiscale simulations linking genotype to phenotype, via gene networks, by fully exploiting agent-based modeling. The technical details on the framework and its implementation are provided in the Methods section. Here, we illustrate a study where four setups of increasing complexity are considered, evaluating the impact of new elements in a controlled fashion. **(A)** We simulate the effect of introducing gene network perturbations (activating, +, or inactivating, -, mutations) in single clones. **(B)** We grow mono-clonal or multi-clonal populations of cells in a 3D environment (spheres visually represent single cells). **(C)** We study competition between different clones grown together (colors represent different mutation profiles; the growth curve demonstrates exponential growth of aggressive clones; 2D simulation shows growth patterns under competition). **(D)** We enable interaction with the surrounding microenvironment, e.g., oxygen concentration variation that results to necrotic cells. **(E)** We enable signaling between cells (represented here as tiny black spheres produced by activated cells; junctions represent receptors).

rameter values for the individual elements of the model based on previously published data (see sections below). We then carry out sensitivity analysis to understand the implications of these choices for our specific case.

Cells as computational agents

Cells are represented in microC as computational agents acting and interacting in a 3D space. Cells are arranged in a rectangular 3D grid where each voxel may be occupied by only one cell. They may interact with the microenvironment by consuming oxygen and with other cells via diffusible substances such as cytokines, chemokines, and growth factors/hormones, whose production is defined by the network dynamics. The parameters regulating these aspects of the physical microenvironment, namely, the grid dimensions, the presence of neighboring cells, and local chemical concentrations, can be customized based on specific assumptions suitable for the system to be modeled (the details for each parameter are discussed in the following sections). These assumptions give rise to certain aspects of physical dimension and spatial competition among cells. Furthermore, cells are also meta-agents, namely, each cell is itself populated by a community of computational agents, the genes and molecules, that act and interact as a network inside the cell agent.

Cell mutation profiles

The microC modeling framework enables to input of mutation profiles, representing the specific mutations present in each simulated clone. Thus, it might be used to represent the clonal make-up of specific samples, such as 3D mixed-population cellular spheroids. Mutation profiles can be defined via an input file uploaded to microC. Such files define the (sub)population of cells where specific gene mutations are present. By default, if no mutation profile is provided, the status of each gene in each cell is initialized randomly as active/inactive. If a mutation profile has been defined, this random initialization is overwritten by the specific mutations. The mutations are introduced in the model as constraints on the gene status, such as a constantly active/inactive status (e.g., constitutively activating or inactivating mutations) or they can be introduced as a change in the rules regulating the gene behavior (e.g., amplified or conditional behavior). There is no limitation with respect to the number of mutation profiles that can be simulated simultaneously or the number of mutated genes. In the extreme case, each cell can have a distinct mutation profile, and multiple mutations can occur in each gene of the encapsulated network.

Subcellular gene networks

Gene networks are encapsulated within cell agents and drive their decisions. Although any type of network model may be used in this framework, our current implementation exploits

logical Boolean networks. The latter have been shown to preserve key dynamic characteristics of the gene network [27], and they can be designed quickly, without the need for accurate estimates for a large number of parameters. Briefly, the (gene) nodes of such logical networks can be in active or inactive state. Nodes may be connected with other nodes via links. All nodes are assigned logical rules that determine the current and future state of the node. We use asynchronous network update, first described by Thomas [28] and widely adopted in Boolean gene networks. We distinguish between four types of nodes: genes, receptors (input), output nodes, and fate-decision nodes. Genes have both incoming and outgoing links, receptors have only outgoing links, and output and fate-decision nodes have only incoming links. Cell-fate decision nodes have a crucial role in the simulations as they trigger the actions that determine the cell behavior.

In the specific model developed here, we considered as a starting point a previously developed large mitogen-activated protein kinase (MAPK) network [29]. This is a Boolean network that has been assembled in a knowledge-driven, mechanistic manner by considering gene-gene relations (e.g. activation/repression) as reported in the published literature. As such, this network is not specific to a given context, cell line, or genotype; however, it is likely to be somewhat biased towards signaling and interactions observed in cancer cell lines, as the pathways modeled are key to the hallmarks of cancer. We then extend this network to introduce a hypoxia responsive module; this new module and the full network can be explored in Fig. 3 of the Supplementary Protocol File and in the online documentation.

Cell status and cell-fate decision rules

An activated cell-fate decision node is associated with a specific action. Our current implementation of the framework includes the following possible actions:

- Proliferation. A copy of the cell is introduced into a neighboring slot. If all neighboring slots are occupied, the cell enters the growth arrest state. This may be modified in future versions of microC in order to allow for different degrees of cellular constraints: from loosely bound cell masses to tightly bound spheroids. The cell-fate decision node is reset and the cell may enter another round of network simulation, and proliferate again, or chose another cell-fate decision. Indefinite proliferation is unlikely to happen due to spatial constrains (all neighboring slots will be occupied at some point) that will in turn force the cell into a growth arrest state.
- Apoptosis. The cell dies and is removed from the simulation.
- Necrosis. The cells dies; it remains in the simulation and occupies space but it does not otherwise actively participate.
- Growth arrest. The subcellular network simulation for a cell in growth arrest is "paused" for a given period of time. In the specific model presented here, we choose three rounds of simulations. Furthermore, the cell interacts with the microenvironment at a reduced rate. In the specific model presented here, the consumption rate drops to half of the normal rate.
- No decision. The cell takes no action; the simulation continues until a decision is made.

Actions associated with apoptosis and necrosis are executed immediately after the cell-fate decision has been made, whereas actions associated with proliferation and growth arrest decision are executed shortly after the end of a time frame defined by the

user (we name this the *decision window*). During this time frame, the network in each cell is simulated, and the activation status of cell-fate decision nodes may change.

A spatially aware environment

One of the most novel aspects of microC is that cell-microenvironment and cell-cell interactions are modeled via exchange of diffusible substances between cells or between a cell and its microenvironment. Importantly, the environment in microC is modeled as computational agent patches. Concentrations of the diffusible substances are transferred through step functions and may activate receptor nodes of the network. Those receptors may in turn trigger an autocrine or paracrine interaction, influencing cells towards specific cell-fate decisions or the production of certain substances defined by output nodes.

Of note, in microC each 3D voxel is defined as an agent. These voxel or "patch" agents are assigned rules which define their geometry, the interaction with the cells they contain and how they communicate with other voxel agents. This means that different parts of the environment could be defined by different patches, hence, different rules. However, in our initial model and implementation, the rules are set as equal for all voxels (e.g. shape, size, number of cell per patch, diffusion). Cell-microenvironment (cell agent-voxel agent) interactions are associated with a list of environmental resources (e.g. oxygen and growth factors), whereas cell-cell interactions may be the result of user-defined substances, such as cytokines, chemokines, growth factors, and hormones. Diffusible substances are also simulated in microC as agents, and their behavior is simulated following the diffusion—reaction equation:

$$\frac{\partial u}{\partial t} = D_u \, \nabla^2 u + S_u \qquad (1)$$

where u is the concentration of the diffusible substance, D_u is the diffusion coefficient of substance u, and S_u are sources or sinks of the diffusible substance. The equation is solved numerically using an explicit forward time central space scheme, with Dirichlet boundary conditions, on a two-dimensional (2D) or 3D rectangular lattice. The grid cell size may be adjusted to include 1 ($1 \times 1 \times 1$) or 27 ($3 \times 3 \times 3$) cells using the "grid sparsity" parameter.

Cells are modeled as sinks that consume oxygen at a rate proportional to the local oxygen concentration. In particular, oxygen consumption is modeled through the equation:

$$S_{O_2} = R_0 \cdot \frac{C - C_{N,f}}{C_{O_2,opt} - C_{N,f}} \qquad (2)$$

where R_0 is the initial consumption rate, C is the concentration of oxygen in the specific grid cell, $C_{N,f}$ is a threshold value that determines the lowest possible oxygen concentration (currently fixed at 80% of the oxygen activation threshold), and $C_{O_2,opt}$ is an optimal oxygen concentration, currently set to 0.28 mM. The latter two parameters have predetermined values in microC, whereas the initial consumption rate (R_0) and the oxygen activation threshold may be set by the user. The latter is a precondition that triggers the necrotic cell-fate decisions. We set the necrosis threshold at 0.02 mM [23]. Cells in growth arrest consume oxygen at half the initial rate, whereas necrotic cells do not consume oxygen. Parameters such as the diffusion coefficient and the initial/boundary conditions of oxygen concentration can be adjusted as required by the specific application.
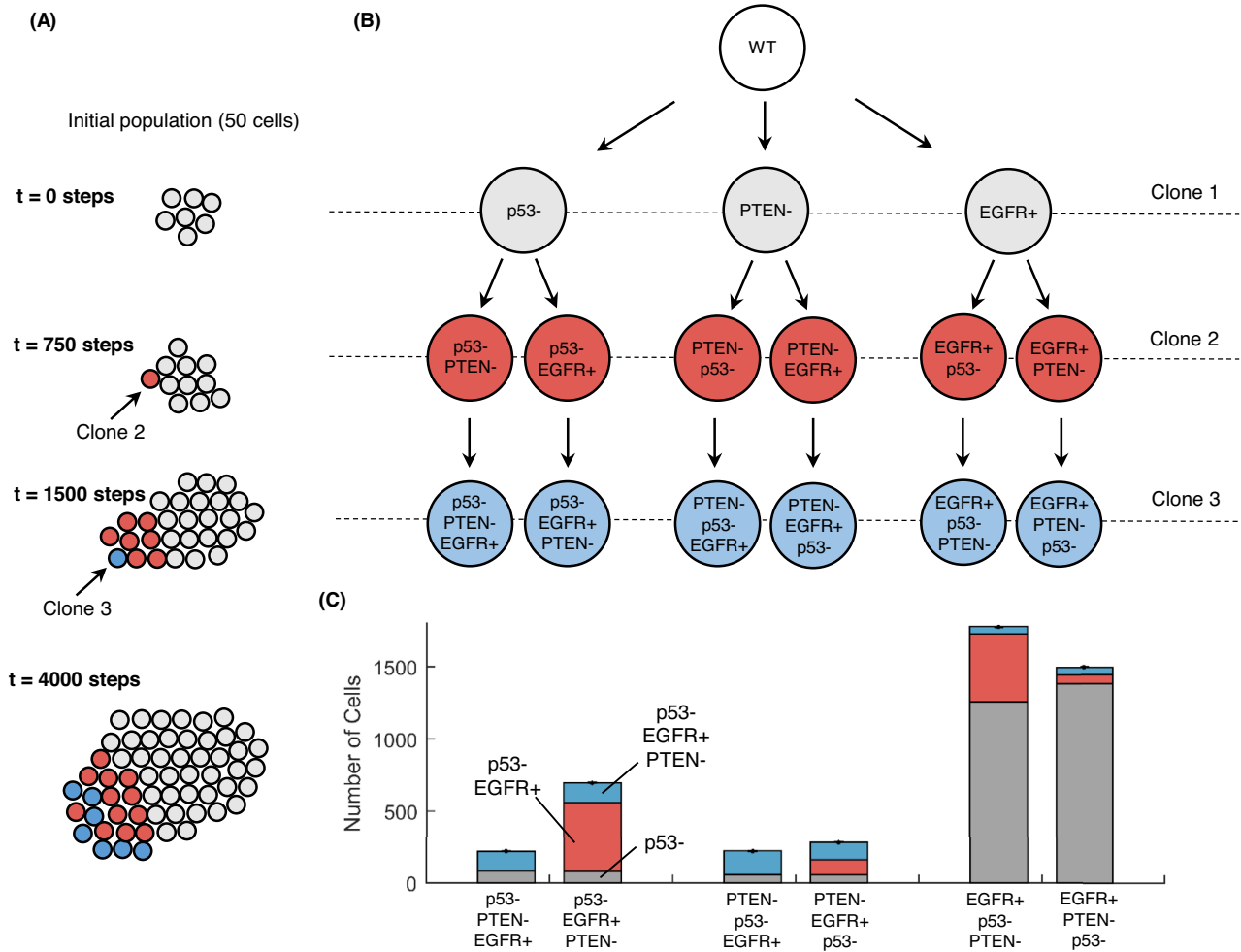
Figure 3: Paths of clonal evolution: the order in which mutations occur affects spheroids' growth. **(A)** Experimental setup. The experiments start with 50 cells of the same clone (Clone 1, shown as gray spheres). At time point t = 750, we introduce a mutation to one cell (Clone 2, shown as red spheres), and at time point t = 1,500 we introduce an additional mutation to a cell of type Clone 2 (that we call Clone 3, shown as blue spheres). We extend the experiment up to 4,000 simulation steps. **(B)** There are six potential combinations in which the three mutations (p53-, PTEN-, EGFR+) can occur. **(C)** The total and clonal subpopulations are shown in the stacked bar chart. Bars are averages of 100 repeats and error bars represent the standard error.

Cell-cell interaction is modeled using the diffusion—reaction equation (equation 1], with S_u representing the sources and sinks (cells) of hormones, cytokines, and any user-defined diffusible substance.

$$S_{diffusables} = R_0 . I_{ijk}^{receptor} + P_0 . I_{ijk}^{output} \qquad (3)$$

Both the consumption of diffusible substances (consumption rate: R_0) and the production of these substances by cells (production rate: P_0) are defined by the user and considered to be constant. Production/consumption of diffusible substances is conditional to the activation status of the corresponding receptor/output node, shown here as a Boolean function $I_{ijk} = 0/1$, with i, j, and k denoting the position of the cell in the 3D lattice.

Spheroid growth measures

In our growth curve simulations, we use the number of cells as an indicator of the size of the spheroids at any given time, and we have used sphericity to assess their degree of roundness:

$$\psi = \frac{\pi^{\frac{1}{3}}(6V)^{\frac{2}{3}}}{A} \qquad (4)$$

where ψ is sphericity, V is the volume of the object, and A its surface area. The radius of a spheroid is determined at each stage of growth as the average distance between the coordinates of the initial center point of the simulation and the outermost cells of the growing spheroids.

Cloud Implementation

The models presented in this study are freely accessible via a web interface [30]. This interface also enables modification of the models and input parameters to conduct experiments other than those discussed here. We have prepared a detailed protocol (Supplementary Protocol) that explains how to submit experiments and how to interpret the results. Briefly, the interface allows a user to upload input parameters to set the model (e.g., mutation profiles for the cell populations, inner-cell gene net-

works, specific values for diffusion, and other kinetic and simulation parameters). It then makes it possible to monitor experimental results in time and to perform statistical inference on the results. Experiments are specified via a web interface (see Supplementary Protocol), where the user may set a number of numerical parameters via sliders. Specifications of the gene network, mutations, and other parameters can also be uploaded from the same page. The gene network can be specified as a Graph eXchange Language (GXL), Graph Markup Language (GraphML), or Ginsim Markup Language (GINML) file. GXL is a widely used XML-based standard exchange format for sharing data; it is a flexible data model that can be used for object-relational data and a wide variety of graphs [31]. GraphML is another XML-based, widely used, data sharing format for graphs [32]. GINML is an extension of GXL and can be produced, e.g., by the logical model editor GINsim [14]. The web server converts any of the above formats to the GraphML format and then submits the experiment as a set of jobs to the Advanced Research Computing Cloud (University of Oxford). Experiments are then executed exploiting the NetLogo framework [33]. Each node runs 16 repetitions of the experiment on each of its central processing unit cores. When all the simulation runs have finished, an hypertext markup language (HTML) file containing both the data and JavaScript interactive data visualizations is assembled, and a link to the page is sent by email to the user. The URL to the results is automatically generated and is private to the user who can choose to share it. Of note, by implementing microC as a cloud service with a web interface for both submitting experiments and analyzing the results, we have automated a great deal of technical and tedious work. Files are automatically converted to the necessary formats, pre-defined scripts are used to run the experiments on the cloud, and JavaScript on the results page provides interactive visualizations of the data, data analysis, and animations of the cellular model and the gene networks.

Results

In silico growth of a heterogeneous population of cells communicating within a 3D microenvironment

We present a modeling framework, microC, that enables simulations of individual cells or group of cells, where each cell contains an inner gene network that simulates the cascade of signaling events occurring in each cell upon stimulation and determines the cell behavior (Fig. 1). To illustrate microC, we report the different ways in which it can be applied (Fig. 1 A-1E). Choosing cancer spheroids as a model system, we illustrate how a specific model can be constructed from its individual elements; we carry out simulations under different perturbations (e.g., mutations, nutrients availability); we discuss how our predictions agree or disagree with results from wet-lab studies; and we conduct sensitivity analyses to assess the impact of the different parameter choices on the model predictions.

As an initial step, we assessed our ability to import the required gene networks and confirmed the faithfulness of our ABM encoding of these networks. We then scaled up the simulation by increasing the genetic and microenvironmental heterogeneity in a stepwise manner. Specifically, we considered a population of homogenous pre-cancerous cells growing in a 3D environment; then, we gradually introduced mutations in onco- and tumor suppressor genes (Fig. 1A) to study how they affect the multi-cellular growth (Fig. 1B). Subsequently, we allowed the resulting clones (carrying different single or multiple mutations) to grow in competition (Fig. 1C) and studied the param-

eters affecting their evolution. Finally, we investigated the additional effects of introducing extrinsic perturbations, such as lack of oxygen and presence of growth factors, and enabling cell-microenvironment (Fig. 1D) and cell-cell interactions (Fig. 1E). We report the parameter values chosen for each experiment in Supplementary Table S1, while a more detailed description of the parameters may be found in the Supplementary Protocol and in the online documentation file in microc.org.

Evaluation of the dynamics properties of the inner-cell gene networks

While there is a large number of methods, from traditional statistics to emerging deep-learning approaches, that permit accurate prediction of the behavior of a population of cells given some initial inputs, such methods often constitute a black box when it comes to interpreting the results mechanistically. They emphasize the predictive ability of the model with respect to the study of the possible causative mechanisms of the predicted behavior. In this first example, we show how for each single cell, microC enables monitoring of the paths that have been followed to arrive at a given prediction. In particular, we show how microC enables the study of the dynamical properties of the gene networks within each cell.

Firstly, we verified that microC could correctly import and execute a gene network developed in the GINSim interface [14]. This involves reformatting and recodifying the network so that it can be executed using our agent-based framework (Fig. 2). As we have automated this reformatting and recoding in microC, we needed to check its faithfulness. We asked how intrinsic perturbations, namely, mutations commonly observed in cancer cells and specifically in breast cancer, affect the functioning of the network. To this end, we compared the gene activation profiles across populations of cells carrying different mutations and we determined the differences in the resulting fate of the cell, focusing on the three possible decisions of proliferation, growth arrest and apoptosis. This first simulation showed that we could reproduce the stable configurations (or stable states) that were previously reported for this network in the published stable-state analysis (Fig. 2A and Supplementary Fig. S1A). This illustrates the ability of microC to execute faithfully a previously defined logical network using an ABM approach. Since our protocols are standard, this opens the technical possibility of reusing any such networks developed using the same standard formats.

In addition to the published results, and thanks to the ABM approach, we could also evaluate the probability of occurrence and temporal profile for cell-fate decisions by performing hundreds of replicated simulations (Fig. 2B, Supplementary Figs. S1B, S2). This reveals that not all stable states are equally likely to occur, and it uncovers transient states that would remain undetected in a standard stable state analysis. For example, we found that there was a contained but measurable (7%) probability of proliferation for cells with a single loss-of-function mutation in p53 (p53-) (Fig. 2B). Often transient states have been dismissed as non-biologically relevant. However, if and when they are, or not, is neither a trivial nor fully answered question. Thus, it is important to detect such states in a network analysis and highlight their potential impact on the different fate decisions in order to start to address their relevance.

Effect of mutations on gene network dynamics and multi-cellular growth

The range of abilities, or hallmarks, that a cell needs to acquire in order to progress to become a cancer cell has been extensively described, and the role of somatic mutations in such processes is well documented [9]. However, the chain of events from a sin-

Figure 2: microC simulation of 3D tumor multi-cellular spheroids reveals growth advantage provided by co-occurring mutations. **(A)** Activation status of genes in the MAPK network for the stable states. The states are labeled with the appropriate color (green: proliferation; red: apoptosis; yellow: growth arrest) depending on the cell-fate node activated. Cells with no specific decision are not labeled with any color. **(B)** Detailed activation status for the clone with p53 loss-of-function mutation (p53-). Columns represent genes and rows represent cells (initial population: 100 cells; repeats: 100; length of simulation: 5,000 steps). Pie charts represent probability profiles for cell-fate decisions for each clone. **(C)** Typical examples of spheroids grown in a 3D environment and MAPK network for two of the clones (upper left for WT cells, which grow very little, and right below for EGFR+p53- cells, one of the most aggressive clones). Circle represents the cell boundary, inside network nodes represent gene products (color represents activation status; red is inactive and green active); edges carry the information on the gene-gene interaction (here, green is activation and red is inhibition). **(D)** Clonal growth curves (initial population: 100 cells; repeats: 100; length of simulation: 2,000 steps).

gle mutation occurring in a normal cell to the acquisition of such hallmarks, and then to the occurrence and progression of cancer, is extremely complex and not fully understood. Here, we used microC to dissect such questions by asking how the occurrence of single and multiple mutations might impact on the behavior of signaling networks and how this results in different patterns of single-cell and multi-cellular growth.

We focused on mutations frequently occurring across cancer types, namely, loss-of-function/inactivating mutations in the well-known tumor suppressor genes p53 and PTEN, and the activation of the known cancer driver EGFR. We then monitored the 3D growth patterns of cells where these mutations were introduced as single mutations (EGFR activating mutation, EGFR+; p53 loss-of-function, P53-; or PTEN inactivation, PTEN-) or in combination of two or three. We compare the resulting growth curves with those predicted using wild-type (WT) cells, namely, cells not carrying any of these mutations. Of note, for these initial simulations, we consider a media with no growth factors or other added nutrients, simulating a condition of cell starvation (see Supplementary Table S1 for all parameter choices).

In these conditions, our model predicts that clones carrying multiple mutations are characterized by a significantly more aggressive phenotype with faster growth with respect to clones carrying single mutations in these genes (Fig. 2C and 2D, Supplementary Fig. S3). Furthermore, our model predicts that activated EGFR signaling is a determinant for rapid growth under starved conditions. Specifically, in our simulations, all EGFR+ clones (EGFR+, EGFR+PTEN-, EGFR+p53-, EGFR+p53-PTEN-) exhibited initial exponential growth while clones with no activated EGFR signaling did not grow or grew at a much slower rate (Fig. 2D).

To assess the usefulness and plausibility of our predictions, we considered experimental data obtained using cells where mutations in EGFR, p53, and PTEN have been induced either alone or in combination. We asked how an initial general model, not specifically built for any cancer types but built in a mechanistic fashion using hundreds of independent publications on gene interactions, could provide useful predictions with respect to published studies not used in the model building. Specifically, we considered results from a study using MCF10A, an immortal though not tumorigenic mammary tumor cell line. This model has been shown to express markers that are associated with the basal-epithelial phenotype, but it does not carry the mutations frequently observed in this breast cancer type. In these cells, the effect of PTEN deletion, p53 loss-of-function mutation, and EGFR activating mutations on growth and colony formation has been previously measured under conditions of starvation [34, 35]. As shown by Pires et al. [35], these mutations as individual oncogenes could not stimulate growth in 3D culture in soft agar, while the double mutants showed increased growth, and the triple mutant grew significantly more rapidly and formed significantly more colonies than either of the matched double mutants. These experimental results agree with our simulations. We also observed a discrepancy between Pires et al. experiments and our predictions as in their hands PTEN as an individual oncogene could stimulate 2D growth, but not 3D growth, of MCF10A cells in the absence of exogenous growth factors. In our predictions, we did not observe any significant difference between the 2D and 3D growth of the PTEN clones.

We then compare the sphericity as further geometrical property of the spheroids growth in a 3D environment, other than simply size in time. Sphericity is a measure of how near an object is to a perfect sphere (see Methods section). This showed that spheroids formed by the most aggressive clones (higher pro-

liferations rates), namely, EGFR+p53- and EGFR+p53-PTEN-, not only grew faster but they also grew in a more symmetrical manner, with higher sphericity than other clones (Supplementary Fig. S4). This is understandable from a geometrical point of view, as in our model the clones that tend to have proliferation as their main action, rather than apoptosis or growth arrest, can make the best use of the space around them. However, the accuracy of this prediction would need to be confirmed. In this respect, the difficulty of growing some of the less aggressive cell lines means that there is not published evidence on these morphological aspects, and they are hard to assess in an experimental context. However, this is an intriguing result that suggests that morphological characteristics might be a useful aspect to consider in future studies linking the way a spheroid grows with its clonal composition.

Finally, we compared the relative doubling time of the different clones. We observed that the doubling time for the EGFR+ clones (EGFR+, EGFR+PTEN-, EGFR+p53-, EGFR+p53-PTEN-) ranged from 4.1 to 6.9 rounds of simulation, thus it was relatively short, while the rest of the clones did not have the potential to double. These results agree well with results reported in an independent study (not used to train the model) for premalignant MCF10A breast epithelial cells carrying EGFR activating mutations, with respect to WT MCF10A cells [36]. Specifically, EGFR mutant cells showed a relatively short doubling time (20–22 hours) irrespective of the presence of EGF in the media, while cells not carrying a EFGR activating mutation did not reach their doubling time, unless stimulated by EGF.

Scrutiny of clonal evolution paths: significance of the order at which mutations occurs

In the previous examples, we considered the co-existence of multiple mutations. This reflects reasonably well experimental conditions where mutations are artificially introduced, but it might not represent clonal evolution in real tumors. Scrutiny of clonal evolution paths is an emerging field of research; however, this has typically been done without taking into account the signaling and context in which mutations occur. In this example, we ask how the order in which mutations occur affects both individual cells and the overall multi-cellular growth.

Focusing on the aggressive EGFR+p53-PTEN- clone (Fig. 3A), we examine the six possible evolution paths for this clone (Fig. 3A and 3B). This revealed that the order in which mutations occur has a significant effect on a spheroid's growth (Fig. 3C). Specifically, the time of occurrence of the EGFR+ mutation was crucial; clones that acquire this mutation before the loss of a tumor suppressor resulted in larger spheroids, followed by those clones that acquire the EGFR+ mutation as second mutation, and finally those that acquire the EGFR+ mutation as the last mutation (Fig. 3C).

These results confirm first that cancer can occur from multiple evolutionary paths but they also suggest that a proliferation stimulus, namely, EGFR activation, followed by the loss of a tumor suppressor, p53 loss-of-function, and then PTEN loss-of-function, results in the most rapid evolution. This appears to support the preponderance of experimental data indicating that p53 mutation is a relatively late, rather than cancer initiating, event in a number of cancers (see, e.g., [37]). However, the evidence on this point is contrasting, and it is well known that p53 is affected by multiple mutations, with different functional implications (for a review see, e.g., [38]), so further studies are needed to understand the implications of such differences. Importantly, and differently from other approaches to study clonal evolution, microC enables exploration of how differ-

ences in growth rates between cells carrying different mutations might result from the underlying characteristics of the network (Fig. 2 and Supplementary Fig. S5). For example, EGFR activation directly affects the status of a large group of genes, including *ELK1, CREB, MYC,* and *RAS,* that promote proliferation and block apoptosis (Supplementary Fig. S6), and this explain why to acquire this mutation early would be very advantageous.

Finally, growth rates depend also on dynamical network parameters, such as the speed of the specific intercellular processes. We performed a thorough sensitivity analysis by changing the value of the parameters, starting from values suggested in the literature and expanding the range far from this initial choice (see Methods section, Supplementary Material, and Supplementary Figs. S7 and S8). This identified the temporal decision window as one of the critical parameters, which is tightly linked with the temporal ratio between intracellular to intercellular processes. This analysis shows that changes in this parameter can affect the resulting growth rate, and the effect is different when different mutations are considered. As expected, variations in the decision window were reflected by a different number of cells associated with a given cell fate, as more cells could reach a decision when longer windows where allowed. Small decision windows (below 100 steps) showed smaller differences between the growth curves of the different clones; however, at this time, only a small number of cells will have reached a decision (Supplementary Fig. S2), thus the predictions are based on a very small number of cells. For large decision window values, the predictions started to converge, and the choice on the decision window affected the absolute number of cells but not the relative populations, and the ranking of the clones with respect to their ability to proliferate was maintained (Supplementary Fig. S7). This was also reflected in the activation/inactivation profiles for the different states in the different clones, where a value of 100 was the optimal choice in order to preserve dynamical behavior of the model while minimizing computational intensity of the simulations (Supplementary Fig. S8).

Emerging competition patterns impact the growth of multi-clonal cell populations

Next, we asked how competition between different clones, grown together in a 3D multi-cellular spheroid, affects the 3D growth dynamics. To this end, we introduce multiple clones in the same environment (Fig. 4A and 4B) and compare the growth curves of the resulting spheroids (Fig. 4C) and their final size (Fig. 4D) with those observed when the same clones were grown in isolation, that is, in single-clone spheroids.

In the multi-clonal simulations, we reveal that clones with aggressive phenotypes systematically take over the free surface area of the spheroids, thus restricting the rest of the clones in the central parts of the spheroid. This is particularly evident in the 2D geometry (Fig. 4A). This is a striking finding and it implies that the population of the aggressive phenotypes not only increases rapidly against the rest of the clones due to faster growth but it also creates a physical barrier for any further proliferation of the inner, slower-growing population.

This effect significantly affects both the growth curves (Fig. 4C) and the final population fractions (Fig. 4D) achieved by the same clones grown in competition and in isolation. The most aggressive clones (EGFR+p53- and EGFR+p53-PTEN-) increase their presence by 16.7% (EGFR+p53-, from 31.1% of total population in isolation to a 36.3% in competition) and by 27.3% (EGFR+p53-PTEN-, from 33.0% of total population in isolation to a 42.0% in competition). The rest of the clonal populations decrease by

28%–54%. The population of cells that decrease the most (by 54.5%) are the EGFR+ clones.

Interestingly, these findings can be examined in light of the proliferation rates and the dynamical properties of the different clones (Fig. 2B). In particular, EGFR+p53- and EGFR+p53-PTEN- clones are the only ones characterized by a single possible outcome for the cell fate decision, which is proliferation. This is a strong advantage when competing with clones that are characterized by multiple decision outcomes. For example, EGFR+ clones have a higher probability of undergoing apoptosis or growth arrest, which constitutes a strong disadvantage under direct competition since apoptotic events free space that is likely to be rapidly occupied by more aggressive clones.

Interaction between the genotypes and the microenvironment affects multi-cellular growth and clonal selection

Although the mechanisms are not yet fully elucidated, increasing evidence points to a key role of the microenvironment in clonal selection, hence, multi-cellular growth of heterogeneous populations. To illustrate how microC can address this, we focused on hypoxia simulations as this is one of the major microenvironmental differences between cancer and normal tissue [39–42]. Specifically, we aim to study the formation of necrotic cores in larger spheroids (Fig. 5A and 5B) and their growth under artificially uniform well-oxygenated conditions (our *Control* configuration) with respect to growth when oxygen consumption and diffusion are enabled (we refer to this as the *Hypoxia* configuration) (see also Methods section). To achieve this, we consider environmental agents that simulate the diffusion of oxygen in the microenvironment and have the ability to trigger the hypoxia responsive module (see Methods section); we also introduce a new cell fate decision, necrosis, as response to extremely low oxygen concentrations (0.02 mM O_2). We then simulate this model in our control and hypoxia configurations.

Of note, in our network (Supplementary Protocol Fig. S3) the activation of the hypoxia responsive module causes production of EGF by the cell, which can then be sensed by the neighboring cells and activate EGFR. Thus, the normoxia simulation is carried out in the absence of EGF (no production and no prior presence in the environment), while EGF is present in the hypoxia configuration (produced by the cells). Of note, we can modify this element and either dissociate EGF from the receptor (so EGF is present but not sensed, representing for example of a drug treatment inactivating the receptor) or we can decide not to simulate EGF (so EGF is not in the environment, representing a knock-out of the EGF gene). This allows us to check the effect of introducing signaling between cells in the model and, conversely, the effect of interfering with this signaling (Supplementary Fig. S3).

The first simulations described below are carried out with this signaling switched off and simply assess the diffusion parameters and occurrence of necrosis. In the next session, we will evaluate the EGFR and cell-cell signaling component. Interestingly, we observe that EGFR+ clones are the only ones with the potential to outgrow a critical spheroid size that triggers necrosis. For a configuration setup with initial consumption rate 0.005 mM.s^{-1} and diffusion coefficient 10^{-9} m^2.s, the necrotic core that was formed ranged from 20 to 360 cells (Fig. 5C), which is in agreement with previous reports [43]. Accordingly, spheroids with necrotic cores had on average 4.8%–23.6% fewer living cells than spheroids without necrotic cores.

We then study the combined effect of hypoxia (as defined above) and clonal competition (see Section 3). Namely, we introduce all eight clones in the simulation environment and compared growth in isolation and competition under either hypoxic
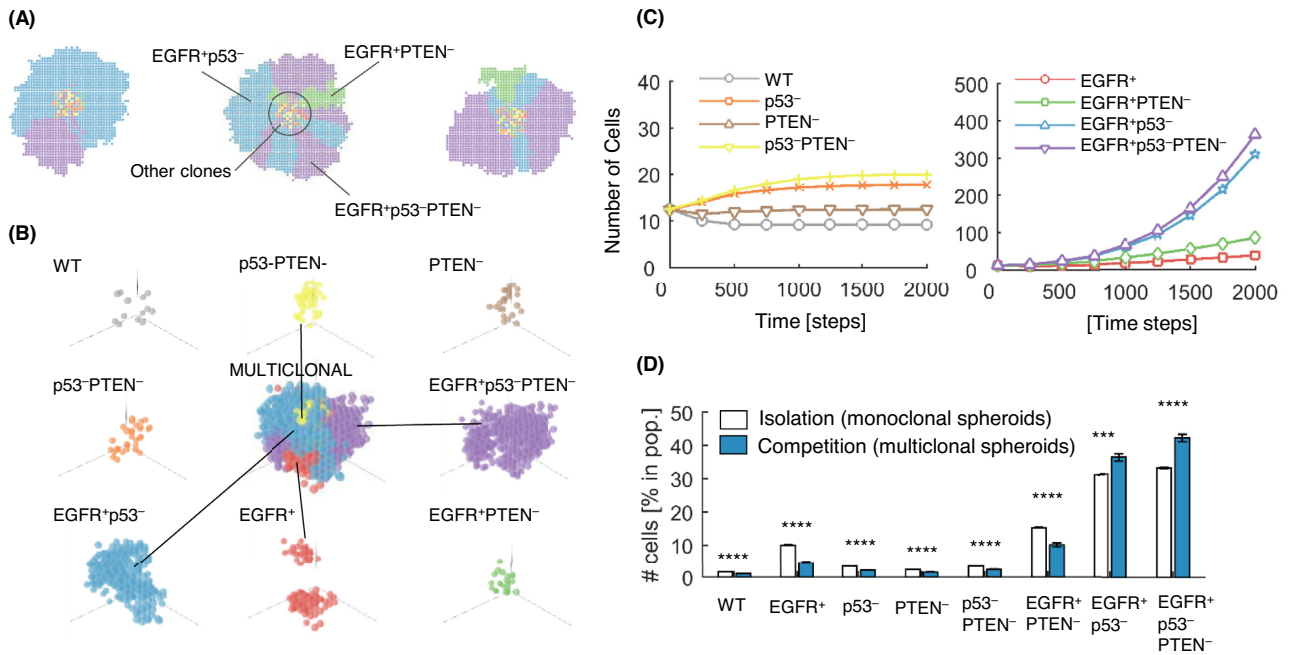
Figure 4: Growth of multi-clonal spheroids is affected by, and in turns affects, the competition between the clones. **(A and B)** Cells with different mutation profiles (colors correspond throughout) are grown within the same virtual microenvironment. At the end of the simulation, each cell type shows a distinct growth pattern. Here, patterns are shown in 2D and 3D. **(B)** A spatial decomposition of a multiclonal spheroid to demonstrate the distribution of the different clonal populations within the spheroid. **(C)** Growth curves of clones under competition in 3D simulations. **(D)** Relative clonal population (over total population of cells) under isolation and competition in 3D simulations. Results are averages of 100 repeats of an initial population of 100 cells. Under competition, the initial population was shared in equal parts among the eight clones. Error bars in bar charts represent standard error. ∗ indicates Kruskal–Wallis $P<0.05$, ∗∗ $P<0.01$, ∗∗∗ $P<0.001$, ∗∗∗∗ $P<0.0001$.

or control conditions (Supplementary Fig. S9). Overall, our simulations showed that spheroids where hypoxia was enabled had reduced clonal diversity (Fig. 5D). In particular, we noticed that the EGFR+p53- and EGFR+p53-PTEN- clones increased their presence in the total population. This was additional to the initial enrichment of this population due to competition (white bar series in Fig. 5D). On the contrary, the rest of the clones decreased their presence in the spheroids by an average of 4%–5%. This selection pressure and consequent reduction of clonal diversity due to hypoxia can be explained by the spatial distribution of clones (Fig. 4A). Less aggressive clones are more likely to be segregated to the central part of the spheroids that eventually will become necrotic under hypoxia. Of note, in this example we have not introduced possible mutations which might occur as a result of hypoxia and could impact on the observed clonal diversity.

Finally, we perform a sensitivity analysis on the parameters involved in the diffusion-reaction equation (Equation 1), namely, we change the oxygen consumption rate and the diffusion coefficient to one of a broad range of values (Supplementary Fig. S10). We found that the consumption rate was the only parameter that, when changed, significantly affects oxygen concentration (Supplementary Fig. S10A), which may impact spheroid growth indirectly by triggering necrosis. This prediction is in agreement with previous evidence showing oxygen consumption to be the most critical kinetic parameter [43].

Impact of cell-cell signaling on multi-cellular growth in a heterogeneous microenvironment
Our final example asks how accounting for cell-cell interaction affects the growth of spheroids. This experiment highlights one of the most innovative aspects of microC. As cell signaling and

its relevance for normal development and disease are increasingly understood, a framework that enables such modeling and study of the consequences of such signaling on cell behavior is correspondingly advantageous.

We study EGF signaling (Fig. 5E), a response triggered by many stress factors, including hypoxia. We compare growth under two experimental conditions: oxygen diffusion simulations with disabled EGF signaling (which we call *Hypoxia—no signaling,* the same as *Hypoxia* in section 5) and oxygen diffusion simulations with enabled EGF signaling (which we call *Hypoxia—signaling*), thus where the cells are producing growth factors that are sensed by the nearby cells. For this experiment we used clones that did not constitutively activate EGFR.

We observed a significant increase in the population of cells under the *Hypoxia—signaling* condition. This increase ranged from 130 to 870 living cells, that is 26%–174% of the spheroid size (Fig. 5F). These effects were consistent with the aggressiveness of the clones that we have seen in the previous examples; namely, p53- and p53-PTEN- clonal populations increased significantly more than the PTEN- and WT clones under hypoxia when EGF signaling was accounted for. Interestingly, enabling EGF signaling between cells further increased the tendency of hypoxia to reduce clonal diversity (Fig. 5D and 5G). This reveals that the reduction in clonal diversity attributable to central necrosis (Fig. 5D) is further increased due to the different proliferation rates of clones that are sensing EGF released under hypoxia.

A sensitivity analysis of the parameters determining the strength and the length of the EGF response, namely, the activation threshold of the stimulus receptor and consumption rate of the growth factor, showed that low activation threshold values are more likely to activate the EGF receptor for any given EGF concentration above the threshold value, whereas lower con-
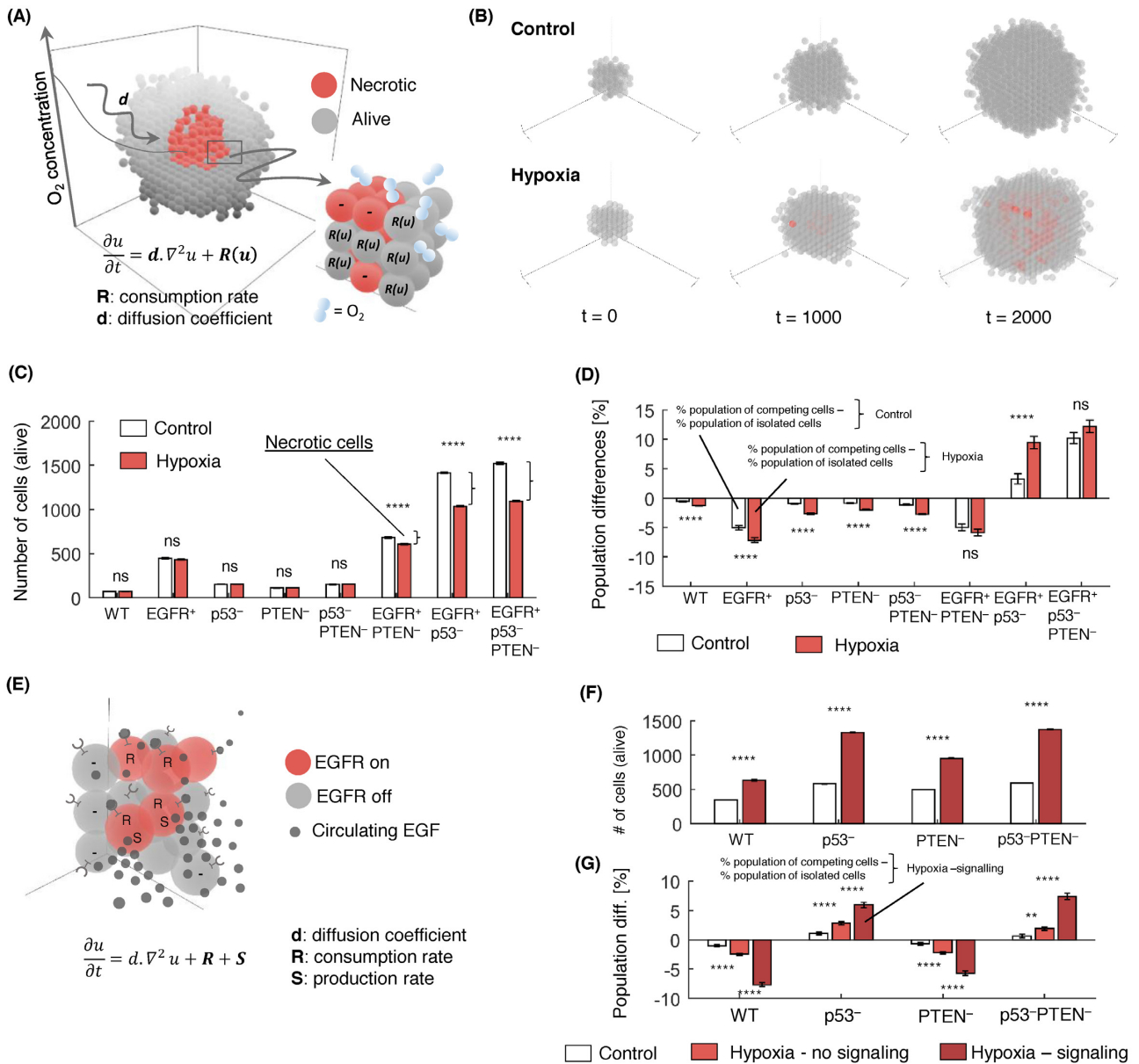
Figure 5: The effect of a hypoxic microenvironment and cell-cell signaling on multi-cellular growth. **(A)** Necrotic core within a spheroid as a result of oxygen consumption by cells. Necrotic cells do not consume oxygen (-), in contrast to living cells (R: oxygen consumption rate). Oxygen diffusion is simulated by the diffusion-reaction equation (Equation 1, in Materials and Methods section). **(B)** Spheroids growing under artificially well-oxygenated conditions (*Control*, initial and boundary condition: 0.28 mM O_2) and an environment with oxygen level drop in the inner layer of the 3D spheroid due to diffusion (*Hypoxia*, initial and boundary condition: 0.04 mM O_2). **(C)** Growth under the well-oxygenated (Control) condition and the hypoxic condition (Hypoxia) for eight clones. EGFR+ clones develop necrotic cores under the hypoxic condition (differences between white and red bars (right braces) show the number of necrotic cells). **(D)** Differences in clonal population fractions (*in silico* living cells) between cells grown isolated and in competition with each other under well-oxygenated condition (Control) and the hypoxic condition (Hypoxia). Bars are averages of 100 repeats (initial population: 100 cells, experiment length: 2000 temporal steps, $R_{O2} = 5.0e\text{-}3$ mM. s^{-1}, $D_{O2} = 1.0e\text{-}9$ m. s^{-1}), and error bars represent standard error. ∗ indicates Kruskal–Wallis $P<0.05$, ∗∗ $P<0.01$, ∗∗∗ $P<0.001$, ∗∗∗∗ $P<0.0001$. **(E)** EGF signaling between cells. Red-colored cells have activated EGF receptors, whereas gray-colored cells have inactivated EGF receptors (junctions on cells). EGF molecules (small, black spheres) are produced (S: EGF production rate) by cells and may be consumed (R: EGF consumption rate) by activating the EGF receptor of the same or a neighboring cell (spheres attached to the EGF receptors), thus promoting proliferation. Cell-cell interaction is simulated by the diffusion-reaction equation (see Material and Methods section). **(F)** Spheroids grown with disabled EGF signaling (*Hypoxia—no signaling*), and with enabled EGF signaling (*Hypoxia—signaling*, 0.04 mM O_2, $ACT_{EGF} = 5.0e\text{-}4$ (+). m^3, $R_{EGF} = 5.0e\text{-}4$ (+).$m^3.s^{-1}$, R_{O2} and d_{O2} as above), initial population: 500 cells, experiment length: 2,000 temporal steps. The initial and boundary configuration under Hypoxia is 0.04 mM O_2. Bars are averages of 100 repeats. Error bars represent standard error. **(G)** Relative clonal populations in isolation and competition under different oxygen configurations (Control [Normoxia], Hypoxia—no signaling, and Hypoxia—signaling). Percentages are normalized for each condition to the number of living cells at the end of the simulation across the four cell types. Bar charts are averages of 100 repeats (initial population 500 cells, 2,000 steps). Error bars represent standard error. ∗ indicates Kruskal–Wallis $P<0.05$, ∗∗ $P<0.01$, ∗∗∗ $P<0.001$, ∗∗∗∗ $P<0.0001$. (+) fraction of the EGF production rate.

sumption rates of EGF are more likely to activate the EGF receptor for longer (Supplementary Fig. S10B). Both events increase

the probability of proliferation that in turn affects the size of the spheroid (Suplementary Fig. S10C).

Discussion

To respond to the need to deepen our understanding of the intricate relationship between cell genotype and phenotype, we have developed microC, which combines a powerful stochastic method, ABM, and gene network modeling into a novel framework for *in silico* experimentation. Specifically, microC addresses the challenge of modeling and simulating the dynamics and evolution of a heterogeneous population of cells within a changing microenvironment. ABM is increasingly used to simulate the dynamics and evolution of complex systems in applications ranging from engineering to ecology [44–47]. This approach makes microC a naturally multiscale framework, enabling assessment of both multi-cellular systems and individual cells, together with their physical and molecular properties.

One of the most innovative aspects of microC is that it substantially extends the capacity of ABM simulations of living cells, considering each individual cell as a *meta-agent*. Each cell is considered as a community of computational agents, the genes and molecules, acting and interacting within each cell. This enables the user to modify and/or replace gene networks in the cells, to define new constrains representing different types of mutations in different cells or in the same cell, and to customize cell-cell and cell-microenvironment interaction parameters. As a consequence, the proposed framework is naturally suited to study how the behavior of a specific perturbation, such as a mutation, occurring in individual cells within a 3D dynamic microenvironment, affects the collective behavior of other, similar or different, cells and the whole system. This reveals in some cases unexpected patterns of collective behavior, not *a priori* defined in the model, that could not be predicted by observing the individual elements. Instead, there are emerging properties of the system as a whole which affect the evolution of the cell population and the behavior of the single elements in return.

microC comes with an example MAPK signaling network that can be used as is, or modified to model in more detail specific pathways, or else be completely replaced with a new one by the user so that it is more specific to the system studied. Using this example signaling network, we illustrated microC features through the study of growth patterns of 3D *in silico* spheroids affected by perturbation of intrinsic (mutations) and extrinsic (oxygen and growth factor availability) factors.

In agreement with experimental results obtained by inducing mutations in the MCF10A pre-cancer model, we demonstrated that clones carrying concomitant mutations in the well-known tumor suppressor genes p53 and PTEN, together with the activation of the known cancer driver EGFR, had a growth advantage with respect to clones carrying single mutations or combinations of any two mutations. We also predict that the order in which these mutations are acquired can have a significant impact on the spheroid growth rate and its final size. Both of these results held true when the clones were grown in isolation and when they were allowed to compete with other clones. We also showed that this effect increased under more extreme microenvironmental conditions, namely, lack of oxygen. Interestingly, we observed that morphological characteristics of spheroids grown from different clones varied considerably and may be a source for significant variability in *in vitro* experiments [48]. We show how the dynamics of a gene network that is specified by the genotype and microenvironmental characteristics affects the proliferation rate that, in turn, has a significant impact on the overall spheroids' size and shape, irrespective of other elements such as adhesion forces, which are long known to affect morphology [49].

Finally, we observed emerging properties of multicellular growth, such as the formation of necrotic cores in the larger spheroids, which have been previously described, and also new unpredicted emerging properties, such as the effect of hypoxia and EGF signaling on the clonal diversity of the spheroids. Importantly, these properties were not encoded at the cellular level but rose from the cell agents competition for nutrients, space, and cellular interaction.

Notwithstanding the modeling possibilities that this novel framework opens, it is important to recognize that the current implementation of the methodology has some limitations. Firstly, although microC accounts for certain important aspects of physical modeling such as the three-dimensionality, the presence of neighboring cells, and local concentrations of chemicals and molecules, it does not account in its current implementation for physical factors such as matrix porosity, stiffness, and topographical cues. Given the importance of modeling these factors [50, 51], future extension of microC will need to include them. On the other hand, we chose to model the cellular environment using ABM; namely, our 3D voxels are themselves agents whose shape and behavior are defined by rules (see Methods section). These rules can be different for different parts of the environment and can change in time, facilitating the dynamic modeling of physical factors using this framework.

A second limitation of our initial model is that it considers only some possible actions for the cells (e.g., proliferation, growth arrest, apoptosis) and it does not consider, e.g., an important action such as invasion. While enhanced overall proliferation can provide an indication of invasion, and it has has been shown to correlate with migration and invasion capability in multiple cancer cell lines [52], whether specific cells in a spheroid divide or migrate out of the spheroid is an important aspect to address [52, 53]. Thus, we do foresee this as an important future development, and our choice of considering cells as independent computational agents in a ABM framework is ideal and greatly facilitates addition of cell actions such as migration and invasion.

Finally, the use of Boolean networks to represent gene expression and activation is a simplification that can be reasonably applied in the case of loss-of-function perturbations, where a gene is either expressed or not, active or inactive. However, this might not accurately represent subtle changes in expression with different biological implications or mutations that change the gene function instead of simply inactivating the gene. Although it is possible to introduce multiple nodes for a single gene, each one representing a different state, it is natural to extend the current Boolean framework into a logical framework with any number of states covering different levels of expression or different mutations.

In summary, here, we presented for the first time and assessed the capabilities of a novel modeling framework that links genotype with phenotype via gene networks and signaling pathways. We have provided a number of examples of how this framework might be used, illustrating strengths and limitations of the current implementation. Importantly, this framework not only enables a broad range and new types of modeling studies, but it also delivers a microenvironment for *in silico* experimentation built using well-recognized formats and shared standards, thus enabling widely used model representations. This provides an environment for prediction, experimentation, and reasoning using existing gene networks and cell models, as well as a powerful starting point for the development of new ones.

Availability of source code and requirements

Project name: microC

    Project home page: http://www.microc.org

    Operating system(s): Linux

    Programming language: Java, Javascript, Netlogo

    Other requirements: JavaSE 1.7 or higher, GWT 2.7.0 or higher, Tomcat 7.0 or higher

    License: GPLv3.0

    Any restrictions to use by non-academics: none (only as defined by the GPL v3.0 License)

    RRID:SCR_016672

Availability of supporting data

The protocol for this work is available as Protocols.io protocol [26]. Further supporting data and snapshots of the code and visualization data are available in the *GigaScience* repository, GigaDB [54].

Additional files

Protocol.docx

Figure S1. microC's ABM gene network implementation reproduces results obtained with stable-state network analysis. We tested 14 different mutation profiles or environmental stimuli responses. (A) Stable-state analysis as presented in Grieco et al, 2013 (cyclic atractors, ca, are not shown in this graph). The horizontal axis represents the genes in the MAPK network, and the vertical axis represent stable states of different clones (S1 and S2 are multiple stable states). (B) Simulation results with microC. Each row of the heatmaps represents the state of one cell. States are composed by the activations status of genes in the MAPK network, shown in the horizontal axis in the same order they appear in Fig. A. The activation status is coded with colour: grey for activate and white for inactive genes (the last three columns are colour-coded depending on cell-fate decision). Overall there are 10 000 cells shown in each heatmap corresponding to 100 repeats with 100 cells each. The cell-fate decisions (average $\pm$ standard deviation) are shown next to the heatmaps (proliferation: green, apoptosis: red, growth arrest: yellow, and no decision: grey). (Further setup: Number of replicates: 100, Maximum number of simulation steps: 5000, Initial number of cells: 100, Cell decision window: 5001, Network update rate: 1, 3D simulation: true).

Figure S2. Temporal evolution of cell-fate decisions for different clones. Cell fate decisions as a function of time for the same mutations and environmental stimuli as in Grieco et al, 2013. The charts show the fraction of cell-fate decisions (green: proliferation, red: apoptosis, yellow: growth arrest, grey: no decision) in a population of 100 cells at any time point throughout the experiment (5000 temporal steps). At the end of the experiment the results have converged to the stable state analysis published in Grieco et al, 2013. Results are averages of 100 repeats. (Number of replicates: 100, Maximum number of simulation steps: 5000, Initial number of cells: 100, Cell decision window: 5001, Network update rate: 1, 3D simulation.

Figure S3. Growth under Hypoxia, and Hypoxia Signalling. Growth curves for the different clones considered in this study, under different environment conditions. (A) Growth simulating normoxia, starvation conditions (no oxygen, nor EGF diffusion), (B) Growth with oxygen level drop in the inner layer of the 3D spheroid due to diffusion (*Hypoxia*, initial and boundary condition: 0.04 mM O_2, $R_{O2} = 5.0e\text{-}3$ mM.s^{-1}, $d_{O2} = 1.0e\text{-}9$ m^2.s^{-1}), no EGF in the media but EGF produced by the cells is diffused. (C) Hypoxia configuration with disabled EGF signalling (EGF produced but not diffused), and (D) with enabled EGF signalling. Oxygen concentration 0.04mM O_2, $ACT_{EGF} = 5.0e\text{-}4$ ($^+$).m^3, $R_{EGF} = 5.0e\text{-}4$ ($^+$).m^3.s^{-1}. Curves are averages of 100 repeats. (Number of replicates: 100, Maximum number of simulation steps: 2000, Initial number of cells: 100 (500 for hypoxia—signalling), Cell decision window: 100, Network update rate: 1, 3D simulation: true). ($^+$) fraction of the EGF production rate.

Figure S4. Geometrical properties of spheroids depend on proliferation rate of clone. (A) Sphericity for 100 spheroids (< 500 number of cells) for 8 different clones. (B) Significance levels for the differences observed in the boxplot. $*$ indicates Kruskal–Wallis $P < 0.05$, $**$ $P < 0.01$, $***$ $P < 0.001$, $****$ $P < 0.0001$ (C) Correlation between average sphericity and average proliferation rate. We exclude the initial phase of growth (<500 temporal steps), as the cells are initially arranged in an artificial spherical setting. (D) Temporal evolution of average sphericity, and respective size of spheroids for each clone. Results are averages of 10 repeats, and spheroids limited to a maximum of 4000 cells (this is why some experiments are shorter than others).

Figure S5. Dynamical characteristics of cells with loss-of-function mutations in well-known tumour suppressor genes p53 and PTEN, and activation of the known cancer driver EGFR. (A) Stable states analysis of clones with single or co-occurring mutations. S1, S2 refer to multiple states of the same clone. Colours in the last three columns correspond to cell-fate decisions (proliferation: green, apoptosis: red, growth arrest: yellow). (B) Heatmaps show the activation status of genes in MAPK network (horizontal axis). Each row of the heatmap represents the state of one cell. Overall there are 10 000 cells (100 repeats with 100 cells each). The stacked bar charts show the fraction of cell-fate decisions at the cell population (100 cells) at any time point during the experiment. The results are averages of 100 repeats. The cell-fate decisions (average $\pm$ standard deviation) are shown next to the heatmaps for two distinct time points: 100 steps after the experiment starts and, at the end of the simulation. (proliferation: green, apoptosis: red, growth arrest: yellow, and no decision: grey). Number of replicates: 100, Maximum number of simulation steps: 5000, Initial number of cells: 100, Cell decision window: 5001, Network update rate: 1, 3D simulation: true.

Figure S6. Activation status of genes is determined by mutation profile. The MAPK network used in the simulations in both of these cases is the same, yet the mutations profile different. (A) WT cells, and (B) EGFR+p53-. The circle represent the cell boundary. Inside the circle: network nodes represent gene products (colour represents activation status, red: inactive, green: active); Edges represent interactions between genes (red: inhibition, green: activation). Outside the circle: Pink nodes (left) represent receptors (linked with environmental stimuli), and orange nodes (right), represent output nodes (cell products).

Figure S7. Sensitivity analysis for the effect of the multiscale parameter *cell decision window* on growth curves. Growth curves of clones under the same experimental condition, but with different values for the parameter cell decision window (the simulation "cell cycle" time), which regulates the timing of extracellular actions, such as cell-fate decision, with respect to the timing of events internal to the cell, determined by the network execution (shown in the horizontal axis). Curves are averages of 10 repeats that run for 10 cycles. A decision window as small as 100 was sufficient to replicate the same qualitative results (exponential growth for EGFR over-expressed clones, smaller growth for non-EGFR over-expressed clones) that we ob-

served with much higher values of the cell decision window, thus decreasing the simulation time by a factor of 10.

Figure S8. The sensitivity of microC state activation/inactivation when changing the value of the decision window paramater. The decision window is the number of internal (network) steps for every external (inter-cellular) step. Longer internal simulations (large decision window) result to network stable states (figures on the right). Each row of the heatmaps represents the state of one cell. States consist of the activations status of genes in the MAPK network, shown in the horizontal axis. The activation status is coded with colour: grey for activate and white for inactive genes (the last three columns are colour-coded depending on cell-fate decision). Overall there are 10 000 cells shown in each heatmap corresponding to 100 repeats with 100 cells each.

Figure S9. Growth under competition in Hypoxia, and Hypoxia Signalling. We studied growth for 8 different mutation profiles grown under different conditions; in Figure S3 we considered these as monoclonal spheroids, here we grow the clones together in multi-clone spheroids and we study competition between the clones. (A) Growth under competition without considering oxygen diffusion, (B) Growth under competition with oxygen level drop in the inner layer of the 3D spheroid due to diffusion (*Hypoxia*, initial and boundary condition: 0.04 mM O_2), (C) Growth under competition and hypoxia configuration with disabled EGF signalling, and (D) with enabled EGF signalling (Oxygen concentration 0.04mM O_2, $ACT_{EGF} = 5.0e-4$ (+).m³, $R_{EGF} = 5.0e-4$ (+).m³.s⁻¹). Curves are averages of 100 repeats. Interface setup: Number of replicates: 100, Maximum number of simulation steps: 2000 (5000 for hypoxia—signalling), Initial number of cells: 100 (500 for hypoxia—signalling), Cell decision window: 100, Network update rate: 1). (+) fraction of the EGF production rate.

Figure S10. Sensitivity Analysis for the parameters regulating the diffusion processes. (A) Extreme low oxygen concentrations (0.02mM O2), may trigger a necrotic response to cells. Here, we demonstrate the oxygen concentration at the centre of growing spheroids for various values of the initial Oxygen consumption rate (R_0), and the Oxygen diffusion coefficient (d). The experiments are repeated for three different values of the initial oxygen concentration (C_{init}). The line are averages of 10 repeats. (Initial population: 100 cells, 2000 temporal steps). (B) Intensity and duration of an EGF response starting at a single spatial point. The effect is regulated by the activation threshold for EGF receptors (ACT_{EGF}) and the consumption rate of EGF (R_{EGF}). Red-coloured cells receive a sustained EGF stimulus from their environment. (C) Growth under different combinations of the Consumption Rate and the Activation Threshold. Colour represents the number of cells (results are averages of 10 repeats, initial population: 500 cells, clone: p53-PTEN-).

Abbreviations

2D; two-dimensional; 3D: three-dimensional; **ABM**: Agent-Based Modeling; **EGFR: epidermal growth factor receptor;** **GINML**: Ginsim Markup Language; **GraphML**: Graph Markup Language; **GXL**: Graph eXchange Language; **HTML**: Hyper Text Markup Language; MAPK: mitogen-activated protein kinase; PTEN: phosphatase and tensin homolog; WT: wild type.

Competing interests

The authors declare that they have no competing interests.

Contributor Role	Definition
Conceptualization	F.M.B.
Supervision	F.M.B., K.K.
Project Administration	D.V.
Investigation	D.V., F.M.B.
Formal Analysis	D.V.
Software	D.V., K.K., M.H., R.W., F.M.B.
Methodology	F.M.B., D.V.
Validation	F.M.B., D.V.
Data Curation	D.V., K.K.
Resources	F.M.B., D.V., K.K., M.H., R.W.
Funding Acquisition	F.M.B.
Writing—Original Draft Preparation	D.V., F.M.B.
Writing—Review & Editing	D.V., F.M.B., K.K.
Visualization	D.V., F.M.B.

Author contributions Acknowledgements

References

1. Genomes Project C, Auton A, Brooks LD, et al. A global reference for human genetic variation. Nature 2015;**526**(7571):68–74.
2. Shalem O, Sanjana NE, Zhang F. High-throughput functional genomics using CRISPR-Cas9. Nat Rev Genet 2015;**16**(5):299–311.
3. Ritchie MD, Holzinger ER, Li R, et al. Methods of integrating data to uncover genotype-phenotype interactions. Nat Rev Genet 2015;**16**(2):85–97.
4. Lehner B. Genotype to phenotype: lessons from model organisms for human genetics. Nat Rev Genet 2013;**14**(3):168–78.
5. Yi S, Lin S, Li Y, et al. Functional variomics and network perturbation: connecting genotype to phenotype in cancer. Nat Rev Genet 2017;**18**:395–410.
6. Gilman SR, Chang J, Xu B, et al. Diverse types of genetic variation converge on functional gene networks involved in schizophrenia. Nat Neurosci 2012;**15**(12):1723–8.
7. Girard SL, Dion PA, Rouleau GA. Schizophrenia genetics: putting all the pieces together. Curr Neurol Neurosci Rep 2012;**12**(3):261–6.
8. Hanahan D, Weinberg RA. The hallmarks of cancer. Cell 2000;**100**(1):57–70.
9. Hanahan D, Weinberg RA. Hallmarks of cancer: the next generation. Cell 2011;**144**(5):646–74.
10. Karlebach G, Shamir R. Modelling and analysis of gene regu-

latory networks. Nat Rev Mol Cell Biol 2008;**9**(10):770–80.

11. Le Novere N. Quantitative and logic modelling of molecular and gene networks. Nat Rev Genet 2015;**16**(3):146–58.

12. Molinelli EJ, Korkut A, Wang W, et al. Perturbation biology: inferring signaling networks in cellular systems. PLoS Comput Biol 2013;**9**(12):e1003290.

13. Haydarlou R, Jacobsen A, Bonzanni N, et al. BioASF: a framework for automatically generating executable pathway models specified in BioPAX. Bioinformatics 2016;**32**(12):i60–i9.

14. Chaouiya C, Naldi A, Thieffry D. Logical modelling of gene regulatory networks with GINsim. Methods Mol Biol 2012;**804**:463–79.

15. Hoops S, Sahle S, Gauges R, et al. COPASI–a COmplex PAthway SImulator. Bioinformatics 2006;**22**(24):3067–74.

16. Shannon P, Markiel A, Ozier O, et al. Cytoscape: a software environment for integrated models of biomolecular interaction networks. Genome Res 2003;**13**(11):2498–504.

17. Hanahan D, Coussens LM. Accessories to the crime: functions of cells recruited to the tumor microenvironment. Cancer Cell 2012;**21**(3):309–22.

18. Polyak K, Haviv I, Campbell IG. Co-evolution of tumor cells and their microenvironment. Trends Genet 2009;**25**(1):30–8.

19. Orgogozo V, Morizot B, Martin A. The differential view of genotype-phenotype relationships. Front Genet 2015;**6**:179.

20. Gawad C, Koh W, Quake SR. Single-cell genome sequencing: current state of the science. Nat Rev Genet 2016;**17**(3):175–88.

21. Bailey MH, Tokheim C, Porta-Pardo E, et al. Comprehensive characterization of cancer driver genes and mutations. Cell 2018;**173**(2):371–85 e18.

22. DiRenzo J, Signoretti S, Nakamura N, et al. Growth factor requirements and basal phenotype of an immortalized mammary epithelial cell line. Cancer Res 2002;**62**(1):89–98.

23. Jiang Y, Pjesivac-Grbovic J, Cantrell C, et al. A multiscale model for avascular tumor growth. Biophys J 2005;**89**(6):3884–94.

24. Santoni D, Pedicini M, Castiglione F. Implementation of a regulatory gene network to simulate the TH1/2 differentiation in an agent-based model of hypersensitivity reactions. Bioinformatics 2008;**24**(11):1374–80.

25. Wang Z, Birch CM, Sagotsky J, et al. Cross-scale, cross-pathway evaluation using an agent-based non-small cell lung cancer model. Bioinformatics 2009;**25**(18):2389–96.

26. Voukantsis D, Kahn K, Hadley M, et al. microC: A 3D virtual microenvironment for perturbation biology. protocols.io. 2019 https://dx.doi.org/10.17504/protocols.io.wtjfekn.

27. Davidich M, Bornholdt S. The transition from differential equations to Boolean networks: a case study in simplifying a regulatory network model. J Theor Biol 2008;**255**(3):269–77.

28. Thomas R. Regulatory networks seen as asynchronous automata - a logical description. J Theor Biol 1991;**153**(1):1–23.

29. Grieco L, Calzone L, Bernard-Pierrot I, et al. Integrative modelling of the influence of MAPK network on cancer cell fate decision. PLoS Comput Biol 2013;**9**(10):e1003286.

30. microC website. http://microc.org. Accessed 19/02.2019.

31. Holt RC, Winter A, Schurr A (eds). GXL: Toward a standard exchange format. Reverse Engineering, 2000 Proceedings Seventh Working Conference on; 2000, IEEE.

32. Brandes U, Eiglsperger M, Herman I, et al.(eds). GraphML progress report structural layer proposal. International Symposium on Graph Drawing. Springer; 2001.

33. Wilensky U, Evanston I. NetLogo: Center for connected learning and computer-based modeling. Evanston, IL: Northwestern University; 1999, 49–52.

34. Dent P. The multi-hit hypothesis in basal-like breast cancer. Cancer Biol Ther 2013;**14**(9):778–9.

35. Pires MM, Hopkins BD, Saal LH, et al. Alterations of EGFR, p53 and PTEN that mimic changes found in basal-like breast cancer promote transformation of human mammary epithelial cells. Cancer Biol Ther 2013;**14**(3):246–53.

36. Bessette DC, Tilch E, Seidens T, et al. Using the MCF10A/MCF10CA1a breast cancer progression cell line model to investigate the effect of active, mutant forms of EGFR in breast cancer development and treatment using gefitinib. PLoS One 2015;**10**(5):e0125232.

37. Rivlin N, Brosh R, Oren M, et al. Mutations in the p53 tumor suppressor gene: important milestones at the various steps of tumorigenesis. Genes & Cancer 2011;**2**(4):466–74.

38. Kastenhuber ER, Lowe SW. Putting p53 in context. Cell 2017;**170**(6):1062–78.

39. Eales KL, Hollinshead KE, Tennant DA. Hypoxia and metabolic adaptation of cancer cells. Oncogenesis 2016;**5**:e190.

40. Wilson WR, Hay MP. Targeting hypoxia in cancer therapy. Nat Rev Cancer 2011;**11**(6):393–410.

41. Harris AL. Hypoxia–a key regulatory factor in tumour growth. Nat Rev Cancer 2002;**2**(1):38–47.

42. Haider S, McIntyre A, van Stiphout RG, et al. Genomic alterations underlie a pan-cancer metabolic shift associated with tumour hypoxia. Genome Biol 2016;**17**(1):140.

43. Grimes DR, Kelly C, Bloch K, et al. A method for estimating the oxygen consumption rate in multicellular tumour spheroids. J R Soc Interface 2014;**11**(92):20131124.

44. Macal CM, North MJ. Agent-Based modeling and simulation. Wint Simul C Proc 2009:86–98.

45. Matthews RB, Gilbert NG, Roach A, et al. Agent-based land-use models: a review of applications. Landscape Ecol 2007;**22**(10):1447–59.

46. Wang Z, Butner JD, Kerketta R, et al. Simulating cancer growth with multiscale agent-based modeling. Semin Cancer Biol 2015;**30**:70–8.

47. Thorne BC, Bailey AM, Peirce SM. Combining experiments with multi-cell agent-based modeling to study biological tissue patterning. Brief Bioinform 2007;**8**(4):245–57.

48. Zanoni M, Piccinini F, Arienti C, et al. 3D tumor spheroid models for in vitro therapeutic screening: a systematic approach to enhance the biological relevance of data obtained. Sci Rep 2016;**6**:19103.

49. Chen CS, Mrksich M, Huang S, et al. Geometric control of cell life and death. Science 1997;**276**(5317):1425–8.

50. Haeger A, Krause M, Wolf K, et al. Cell jamming: collective invasion of mesenchymal tumor cells imposed by tissue confinement. Biochim Biophys Acta 2014;**1840**(8):2386–95.

51. Ahmadzadeh H, Webster MR, Behera R, et al. Modeling the two-way feedback between contractility and matrix realignment reveals a nonlinear mode of cancer cell invasion. Proc Natl Acad Sci U S A 2017;**114**(9):E1617–E26.

52. Garay T, Juhasz E, Molnar E, et al. Cell migration or cytokinesis and proliferation?–revisiting the "go or grow" hypothesis in cancer cells in vitro. Exp Cell Res 2013;**319**(20):3094–103.

53. Jimenez Valencia AM, Wu PH, Yogurtcu ON, et al. Collective cancer cell invasion induced by coordinated contractile stresses. Oncotarget 2015;**6**(41):43438–51.

54. Voukantsis D, Kahn K, Hadley M, et al. Supporting data for "Modeling genotypes in their microenvironment to predict single- and multi-cellular behavior." GigaScience Database 2019. http://dx.doi.org/10.5524/100543.